3. Rein, M. Phenomena of liquid drop impact on solid and liquid surfaces. *Fluid Dynamics Res.* **12,** 61–93 (1993).
4. Fukai, J. *et al.* Wetting effects on the spreading of a liquid droplet colliding with a flat surface: experiment and modeling. *Phys. Fluids* **7,** 236–247 (1995).
5. Bennett, T. & Poulikakos, D. Splat–quench solidification: estimating the maximum spreading of a droplet impacting a solid surface. *J. Mater. Sci.* **28,** 963–970 (1993).
6. Scheller, B. L. & Bousfield, D. W. Newtonian drop impact with a solid surface. *Am. Inst. Chem. Eng. J.* **41,** 1357–1367 (1995).
7. Mao, T., Kuhn, D. & Tran, H. Spread and rebound of liquid droplets upon impact on flat surfaces. *Am. Inst. Chem. Eng. J.* **43,** 2169–2179, (1997).
8. de Gennes, P. G. Wetting: statics and dynamics. *Rev. Mod. Phys.* **57,** 827–863 (1985).
9. Hayes, R. A. & Ralston, J. Forced liquid movement on low energy surfaces. *J. Colloid Interface Sci.* **159,** 429–438 (1993).
10. Hudson, N., & Jones, T. The A1 projet—an overview. *J. Non-Newtonian Fluid Mech.* **46,** 69–88 (1993).
11. Dontula, P., Pasquali, M., Scriven, L. E. & Macosko, C. W. Can extensional viscosity be measured with opposed-nozzle devices? *Rheol. Acta* **36,** 429–448 (1997).
12. Bird, R. B., Armstrong, R. C. & Hassager, O. in *Dynamics of Polymeric Liquids* Vols 1, 2, pp 495–520 (Wiley, New York, 1987).
13. Tanner, R. I. in *Engineering Rheology* 168–224 (Clarendon, Oxford, 1992).
14. Bergeron, V., Martin, J. -Y. & Vovelle, L. Utilisation de polymères comme agents anti-rebond dan des formulations mises en œuvre en milieux aqueux. French Patent Application 9810471 (1998); International Extension PCT/FR99/02002 (1999).
15. Yerushalmi-Rozen, R., Klein, J. & Fetters, L. J. Suppression of rupture in thin, nonwetting liquid films. *Science* **263,** 793–795 (1994).
16. Yerushalmi-Rozen, R. & Klein, J. Stabilization of non-wetting thin liquid films on a solid substrate by polymeric additives. *Langmuir* **11,** 2806–2814 (1995).

Acknowledgements

D.B. thanks S. Kumar for helpful discussions; and J. Vermant and P. Moldenaers for help with the elongational viscosity measurements. LPS de l'ENS is UMR 8550 of the CNRS, associated with the universities Paris 6 and 7. We also thank the European Commission for their support in the form of TMR project funding.

Correspondence and requests for materials should be addressed to V.B. (e-mail: vance.bergeron@rhone-poulenc.com).

Significant dissipation of tidal energy in the deep ocean inferred from satellite altimeter data

G. D. Egbert* & R. D. Ray†

* *College of Oceanic and Atmospheric Sciences, Oregon State University, Corvallis, Oregon 97331, USA*
† *NASA Goddard Space Flight Center, Code 926, Greenbelt, Maryland 20771, USA*

How and where the ocean tides dissipate their energy are long-standing questions[1] that have consequences ranging from the history of the Moon[2] to the mixing of the oceans[3]. Historically, the principal sink of tidal energy has been thought to be bottom friction in shallow seas[4,5]. There has long been suggestive evidence[6,7], however, that tidal dissipation also occurs in the open ocean through the scattering by ocean-bottom topography of surface tides into internal waves, but estimates of the magnitude of this possible sink have varied widely[3,8–11]. Here we use satellite altimeter data from Topex/Poseidon to map empirically the tidal energy dissipation. We show that approximately 10^{12} watts—that is, 1 TW, representing 25–30% of the total dissipation—occurs in the deep ocean, generally near areas of rough topography. Of the estimated 2 TW of mixing energy required to maintain the large-scale thermohaline circulation of the ocean[12], one-half could therefore be provided by the tides, with the other half coming from action[13] on the surface of the ocean.

Vertical mixing rates in the deep ocean implied by ocean microsctructure[14] and tracer-release data[15] are typically an order of magnitude too small to balance the rate at which dense bottom water is created at high latitudes[12]. It has thus been suggested that much of the mixing required to maintain the abyssal stratification, and hence the large-scale meridional overturning, occurs at localized 'hotspots' near areas of rough topography[4,16,17]. Numerical modelling studies further suggest that the ocean circulation is sensitive to the spatial distribution of vertical mixing[18]. Thus, clarifying the physical mechanisms responsible for this mixing is important, both for numerical ocean modelling and for general understanding of how the ocean works. One significant energy source for mixing may be barotropic tidal currents. The likelihood of this depends *inter alia* on whether enough power is being extracted from the barotropic tides in the likely 'hotspot' regions. Topex/Poseidon (T/P) satellite altimeter data have now made possible accurate mapping of open-ocean tidal elevations[19], and provide a new opportunity to quantify empirically the spatial localization of tidal dissipation.

Here we concentrate on the principal lunar semi-diurnal tide M_2, which accounts for approximately two-thirds of the total planetary dissipation[20], and is the most accurately known tide. This accuracy is needed, because mapping dissipation involves second-order gradients of measured fields and small differences of large numbers.

The barotropic ocean tide satisfies the tidal equations of Laplace, modified to include effects of an elastic Earth and a self-gravitating ocean[21]. These equations embody conservation of momentum and mass for the ocean fluid:

$$\frac{\partial U}{\partial t} + \mathbf{f} \times \mathbf{U} = -gH\nabla(\zeta_{EQ} - \zeta_{SAL}) - F \quad (1)$$

$$\frac{\partial \zeta}{\partial t} = -\nabla\cdot\mathbf{U} \quad (2)$$

Here ζ is the tidal elevation; $\mathbf{U}$ is the volume transport vector, equal to velocity times water depth H; $\mathbf{f}$ is the Coriolis parameter (oriented to the local vertical), and F is a generic frictional or dissipative stress. The forcing is specified through an equilibrium tide ζ_{EQ}, which must allow for the Earth's body tide[21], and an equilibrium-like 'tide' ζ_{SAL} which is induced by the tide's self-attraction and loading[22].

Equations (1) and (2) may be combined and averaged over time to obtain an expression for the local balance between work rate, W, energy flux, $\mathbf{P}$, and dissipation rate, D:

$$W - \nabla\cdot\mathbf{P} = D \quad (3)$$

A number of different explicit forms for this balance appear in the literature[21,23], reflecting various groupings of terms, and different definitions for work and flux (as well as omission of supposed secondary terms like self-attraction). Here we adopt simple expressions for these terms based directly on equations (1) and (2):

$$\mathbf{P} = \rho g\langle\mathbf{U}\zeta\rangle \quad W = \rho g\langle\mathbf{U}\cdot\nabla(\zeta_{EQ} + \zeta_{SAL})\rangle \quad (4)$$

where the brackets $\langle\rangle$ denote time averages, ρ is mean seawater density and g is gravitational acceleration. Note that W represents the mean rate of working on the ocean of all tidal gravitational forces (including self-attraction forces) and of the moving ocean bottom.

Topex/Poseidon altimeter data provide a direct constraint on tidal elevations ζ, and a number of nearly global maps are now

Table 1 Partition of M_2 energy dissipation (in terawatts) between shallow seas and the deep ocean

	TPXO.4a	GOT99hf	TPXO.4b	TPXO.4c	GOT99nf	Prior	Error
Shallow seas	1.60	1.71	1.61	1.62	1.87	1.96	0.06
Deep ocean	0.83	0.74	0.82	0.81	0.57	0.06	0.06
Total	2.44	2.45	2.43	2.43	2.44	2.02	0.01

Results (in TW) are presented for the five empirical estimates discussed in the text, and for the purely hydrodynamic solution used as the prior model for the assimilation. Error bars[28] are for the assimilation solution TPXO.4a. Here shallow seas are defined to include all ocean areas landward of the thin line in Fig. 1b.

available. Comparison to pelagic and island tide gauges suggest[19] accuracies in the open ocean of roughly 1 cm. Given ζ, calculation of ζ_{SAL} is straightforward[22], while the equilibrium tide ζ_{EQ} is of course known to high accuracy. The primary challenge in using equation (3) to calculate D thus lies in finding the volume transports required for equation (4). We estimate $\mathbf{U}$ by fitting equations (1) and (2), along with no-flow boundary conditions at the coasts, in a weighted least-squares sense. Note that the fit cannot in general be exact, because with ζ given the tidal equations are overdetermined. This calculation requires specifying the form of the frictional stress F, so it is crucial to show that the resulting D from equation (3) is insensitive to this assumption. We do this by using two separate tidal elevation solutions based on two distinct approaches, and by varying relevant parameters over a wide range. Five of the resulting dissipation estimates are used below; a more comprehensive set will be published elsewhere.

The key to the stability of these calculations is a proper choice of weights for the least-squares fitting problem. Because equation (2) is just a simple statement of mass conservation and does not depend on any unknown parameters, this equation should be fitted to a precision consistent with the T/P measurements of ζ—to about 1 cm. Larger relative misfits are justified for equation (1) to allow for uncertainties in bathymetry and in dissipation. By relaxing the fit to the momentum conservation equations, we allow the empirically determined T/P elevations to make appropriate adjustments to the dynamical balance. In particular, residuals to equation (1) can formally do work[24] to enhance or reduce dissipation where our *a priori* assumptions about friction are inconsistent with the observed ζ.

Transports could also be estimated by simply substituting ζ into equation (1) and solving for $\mathbf{U}$. But with this approach the fit to equation (1) is exact and all misfit must be accommodated in equation (2). This results in transports that do not conserve mass, and in dissipation estimates that are too noisy to be useful.

The two elevation solutions considered here are denoted TPXO.4 and GOT99, both based on about six years of T/P measurements. For the TPXO.4 solution, we used a variational data assimilation scheme in which both ζ and $\mathbf{U}$ were estimated by directly fitting T/P altimeter data to the tidal equations[24,25]. This requires a prior model for which we used a purely hydrodynamic (time-step) solution with quadratic bottom friction. The fit to equations (1) and (2) was controlled by a non-local, and spatially variable, dynamical error covariance, of three very different forms: for TPXO.4a, the covariances were as described in ref. 25; for TPXO.4b, a spatially uniform covariance was assumed; and for TPXO.4c, dynamical error variances were increased in regions of rough topography.

For the GOT99 solutions, gridded elevation fields[26] ζ were substituted into equation (1) and (2), and $\mathbf{U}$ was estimated by weighted least-squares[27], consistent with the errors in ζ. Bottom stress was parametrized as $F = r\mathbf{U}/H$, with r ranging from 0.0 (no frictional dissipation at all, denoted GOT99nf) to 0.03 m s^{-1} (an inordinately large friction, denoted GOT99hf).

The deduced dissipation estimates TPXO.4a and GOT99hf are plotted in Fig. 1a and 1b, respectively. Note that the colour scale has been chosen to emphasize the pattern of dissipation in the open ocean, and that the scale saturates in some shallow seas where dissipation is generally greatest. In both plots there are some blue patches where the estimated dissipation is negative. This is clearly not physical, and provides some indication of the magnitude of noise in the estimates. Results from the assimilation method are somewhat smoother and overall have a cleaner appearance (that is, fewer blue spots).

Although there are many differences in detail, the two dissipation estimates have many features in common. The areas of intense dissipation expected due to bottom boundary layer drag in shallow seas are clearly evident in both plots (for example, in Hudson Bay and the Yellow Sea; on the European, Patagonian and northwest Australia continental shelves). More interestingly, the estimates exhibit a similar pattern of significant dissipation in the open ocean. For example, dissipation is clearly enhanced in the Pacific Ocean over the Hawaiian ridge, the Tuamotu archipelago, and over the back arc island chains extending from Japan southwards to New Zealand. The western Indian Ocean around the Mascerene ridge and south of Madagascar also exhibits enhanced dissipation in both estimates. The Mid-Atlantic Ridge shows up clearly in the TPXO.4a assimilation estimate (Fig. 1a), especially in the south Atlantic Ocean. Dissipation is also enhanced in this area in the GOT99hf estimates (Fig. 1b), though the pattern is less distinctive.

All of the areas where dissipation is consistently enhanced are characterized by significant bathymetric roughness, generally with

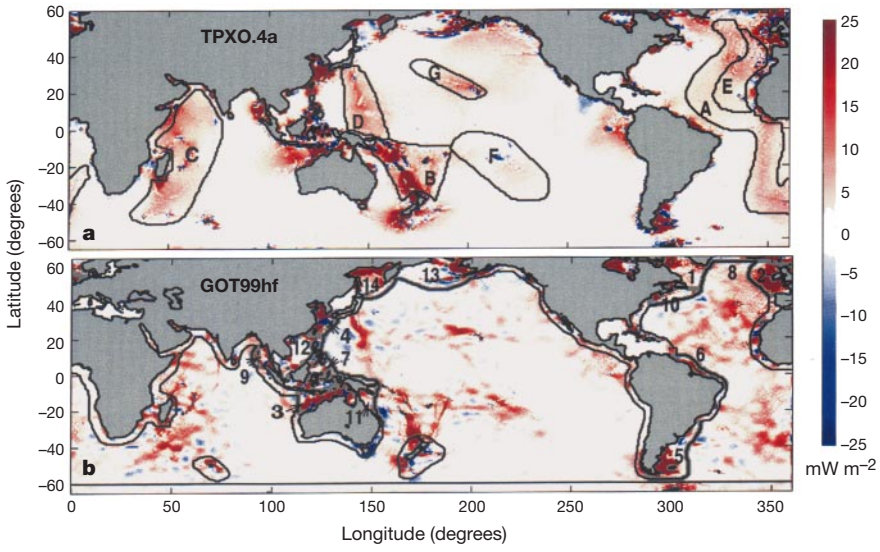

Figure 1 Estimates of M_2 tidal energy dissipation. These estimates of D are computed for two recent Topex/Poseidon (T/P) M_2 tidal solutions. **a**, TPXO.4a elevations and transports, estimated using a variational data assimilation method[25]. **b**, GOT99hf with transports obtained by least-squares fitting[27] of equations (1) and (2) to gridded elevations estimated from the altimetry data[26]. Deep and shallow ocean areas discussed in the text and in Fig. 2 are outlined and labelled in **a** (deep) and **b** (shallow). The thin line in **b** is the boundary between deep ocean and shallow seas.

elongated features such as ridges and island chains oriented perpendicular to tidal flows.

To quantify the large-scale pattern of tidal energy dissipation we consider integrals of D over some larger ocean areas, as outlined in Fig. 1. These integrals can be expressed as a sum of work terms involving integrals of tidal elevations over the whole patch, and line integrals of flux through the boundary of the patch[24]. Only the latter require estimates of transports, so by placing boundaries in deep water the need to estimate currents in shallow seas can be avoided. Total dissipation in shallow seas may thus be accurately determined, even when details of currents in these areas are poorly resolved by the altimeter data.

In Fig. 2a we plot total dissipation for all shelf and shallow-sea areas that account for at least 25 GW of dissipation each. The areas used for these calculations are outlined by heavy solid lines and numbered in Fig. 1b. Results are plotted for all five dissipation estimates—three based on the assimilation solutions, and two based on the weighted least-squares fit to the GOT99 elevations. Also plotted are estimates of error bars for the TPXO.4a dissipation estimates, computed using the Monte Carlo approach described in ref. 28. For most of these major shallow-sea sinks, all dissipation estimates agree within approximately 10–15%; an exception is the complex seas around Indonesia where neither currents nor elevations are well mapped. Note that the region denoted Hudson Bay also includes the Labrador Sea, Baffin Bay and all points north and west.

We also calculated total dissipation in the seven open ocean areas indicated in Fig. 1a as A–G. These are plotted in Fig. 2b. The most significant areas of open ocean dissipation include the Mid-Atlantic Ridge, the western Pacific around Fiji, and the western Indian Ocean. Each of these accounts for approximately 100 GW, comparable to major shallow-sea sinks.

In Table 1 we summarize the partition of dissipation between shallow and deep ocean areas (as defined by the light solid line in Fig. 1b) for the five dissipation estimates of Fig. 2. For comparison, we also include in Table 1 dissipation totals for the purely hydrodynamic prior solution used for all of the assimilation solutions, along with posterior error bars[28] for TPXO.4a. The estimates of global M_2 total dissipation, which in fact depend only on the tidal elevations[21,20], converge to about 2.44 TW, consistent with independent estimates based on space-geodetic techniques, after allowance is made for solid-earth and atmospheric dissipation[29]. The prior solution, which is not constrained by the T/P data, dissipates only 2.01 TW, consistent with results reported for other purely hydrodynamic tidal solutions[23]. Its dissipation occurs only in shallow seas where tidal current speeds are by far the greatest. In contrast, for all of the T/P-constrained solutions a substantial fraction of the dissipation (0.6–0.8 TW out of 2.4 TW, or 25–30%) occurs in the deep ocean.

The TPXO.4a error bars for deep ocean dissipation (0.06 TW) do not cover the full range of estimates in Table 1, and thus do not adequately describe our present uncertainty about the magnitude of tidal dissipation in the deep ocean. The statistical model used for the error calculation was 'tuned' for consistency with observed errors in the data and dynamics[28], and it probably accounts reasonably well for the effects of noise and for limitations in the altimeter data coverage. However, these error bars cannot account for systematic biases which could be implicit in some (or all) of the different estimation schemes. This could particularly be an issue for the GOT99 solutions, which purposely employed a range of frictional drag coefficients far exceeding physically plausible values. Although Table 1 suggests that assumptions about dynamics may have some effect on the final dissipation estimates, similar dissipation totals and a similar large-scale dissipation pattern over the globe are in fact obtained in all cases. Taking account of the formal error bars and the variations between estimates calculated under different assumptions, we estimate that deep sea dissipation for M_2 is approximately 0.7 ± 0.15 TW. The enlarged error bars are probably pessimistic,

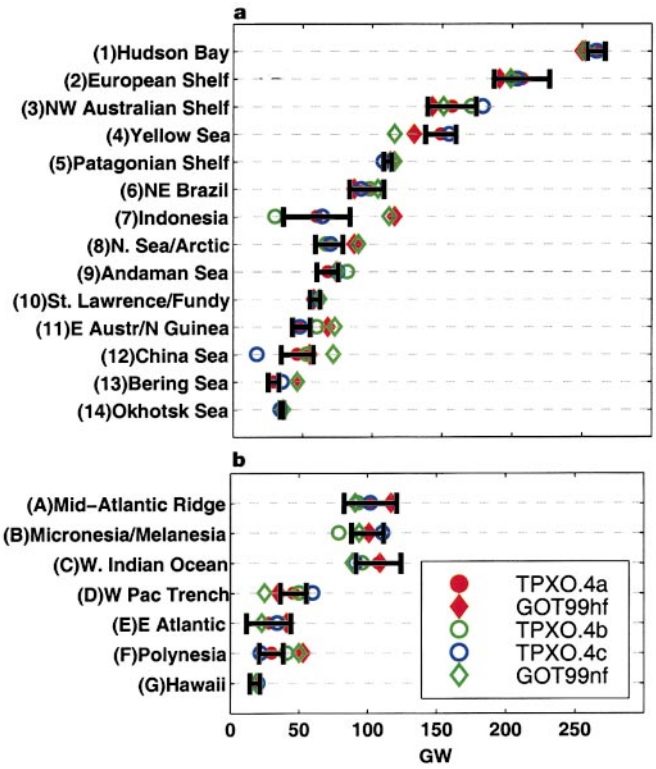

Figure 2 Area-integrated dissipation for selected shallow seas and deep-ocean areas. Results are presented for the five estimates discussed in the text, along with posterior error bars[28] for the assimilation solution TPXO.4a. **a**, Principal shallow-sea sinks of tidal energy. Locations and boundaries of the numbered areas are given in Fig. 1b. **b**, Dissipation in selected open ocean areas, labelled A–G in Fig. 1a.

with the lower limit of 0.55 TW (which is approached only when currents are computed under the unrealistic assumption of no friction) being particularly unlikely.

Although our results do not explicitly constrain the mechanism of open-ocean tidal dissipation, the observed spatial pattern strongly suggests a significant role for scattering into internal tides, induced by tidal flow of the stratified ocean over rough topography[8,10,11]. Indeed, many of the open-ocean areas of high dissipation are known generators of strong internal tides. For example, internal tide observations along the Hawaiian ridge have suggested[30] an energy flux of roughly 15 GW propagating away from the ridge, which is not far from our 20 GW estimate for Hawaii (Fig. 2b). The T/P dissipation estimates are also qualitatively consistent with previous simplified theoretical models[8,11] of internal-tide energetics, although our empirical results suggest that these previous model estimates are somewhat too large.

Extrapolating the results for M_2 to all lunar and solar constituents suggests that approximately 1 ± 0.25 TW of tidal power is dissipated in the deep ocean, probably by scattering into internal waves. This process may also be at work to some extent along the edges of continental shelves (which lie entirely within the area we have classified as shallow sea), so our global estimate is likely to be conservative.

In a recent discussion of the ocean's thermohaline circulation (or, more strictly, its meridional overturning), Munk and Wunsch[12] estimate that 2 TW is needed to maintain the global abyssal density distribution, and they list the possible mechanisms that might provide the required power. They note that the wind provides 1 TW, and ask whether the ocean tides can provide the other. Our answer is that the tides can provide it. But there remain many questions: about the process of barotropic/baroclinic conversion, about the ultimate decay of internal tides into turbulence, and about the implications of these processes for large-scale ocean circulation and climate. □

Received 9 November 1999; accepted 5 April 2000.

1. Munk, W. H. & MacDonald, G. J. F. *The Rotation of the Earth: A Geophysical Discussion* (Cambridge Univ. Press, 1960).
2. Hansen, K. S. Secular effects of oceanic tidal dissipation on the moon's orbit and the earth's rotation. *Rev. Geophys. Space Phys.* **20,** 457–480 (1982).
3. Munk, W. H. Once again: once again–tidal friction. *Prog. Oceanogr.* **40,** 7–36 (1997).
4. Taylor, G. I. Tidal friction in the Irish Sea. *Phil. Trans. R. Soc. Lond. A* **220,** 1–33 (1919).
5. Jeffreys, H. Tidal friction in shallow seas. *Phil. Trans. R. Soc. Lond. A* **221,** 239–264 (1920).
6. Munk, W. H. Abyssal recipes. *Deep-Sea Res.* **13,** 707–730 (1966).
7. Bell, T. H. Topographically induced internal waves in the open ocean. *J. Geophys. Res.* **80,** 320–327 (1975).
8. Morozov, E. G. Semidiurnal internal wave global field. *Deep-Sea Res.* **42,** 135–148 (1995).
9. Wunsch, C. Internal tides in the ocean. *Rev. Geophys. Space Phys.* **13,** 167–182 (1975).
10. Baines, P. G. On internal tide generation models. *Deep-Sea Res.* **29,** 307–338 (1982).
11. Sjöberg, B. & Stigebrandt, A. Computations of the geographical distribution of the energy flux to mixing processes via internal tides and the associated vertical circulation in the ocean. *Deep-Sea Res.* **39,** 269–291 (1992).
12. Munk, W. H. & Wunsch, C. Abyssal recipes II: Energetics of tidal and wind mixing. *Deep-Sea Res.* **45,** 1977–2010 (1998).
13. Wunsch, C. The work done by the wind on the ocean circulation. *J. Phys. Oceanogr.* **28,** 2331–2339 (1998).
14. Gregg, M. C. Scaling turbulent dissipation in the thermocline. *J. Geophys. Res.* **94,** 9686–9698 (1989).
15. Ledwell, J. R., Watson, A. J. & Law, C. S. Evidence for slow mixing across the pycnocline from an open ocean tracer release experiment. *Nature* **364,** 701–703 (1993).
16. Armi, L. Some evidence for boundary mixing in the deep sea. *J. Geophys. Res.* **83,** 1971–1979 (1978).
17. Polzin, K. L., Toole, J. M., Ledwell, J. R. & Schmitt, R. W. Spatial variability of turbulent mixing in the abyssal ocean. *Science* **276,** 93–96 (1997).
18. Samelson, R. M. Large scale circulation with locally enhanced vertical mixing. *J. Phys. Oceanogr.* **28,** 712–726 (1998).
19. Shum, C. K. *et al.* Accuracy assessment of recent ocean tide models. *J. Geophys. Res.* **102,** 25173–25194 (1997).
20. Cartwright, D. E. & Ray, R. D. Energetics of global ocean tides from Geosat altimetry. *J. Geophys. Res.* **96,** 16897–16912 (1991).
21. Hendershott, M. C. in *The Sea* (eds Goldberg, E. *et al.*) 47–95 (Wiley, New York, 1977).
22. Ray, R. D. Ocean self-attraction and loading in numerical tidal models. *Mar. Geodesy* **21,** 181–192 (1998).
23. Le Provost, C. L. & Lyard, F. Energetics of the barotropic ocean tides: An estimate of bottom friction dissipation from a hydrodynamic model. *Prog. Oceanogr.* **40,** 37–52 (1997).
24. Egbert, G. D. Tidal data inversion: interpolation and inference. *Prog. Oceanogr.* **40,** 81–108 (1997).
25. Egbert, G. D., Bennett, A. F. & Foreman, M. G. G. TOPEX/POSEIDON tides estimated using a global inverse model. *J. Geophys. Res.* **99,** 24821–24852 (1994).
26. Ray, R. D. *A Global Ocean Tide Model from TOPEX/POSEIDON Altimetry: GOT99.2* (NASA/TM-1999-209478, Goddard Space Flight Center, Greenbelt, Maryland 1999).
27. Ray, R. D. Inversion of oceanic tidal currents from measured elevations. *J. Mar. Sys.* (submitted).
28. Dushaw, B. D. *et al.* A TOPEX/POSEIDON global tidal model (TPXO.2) and barotropic tidal currents determined from long range acoustic transmissions. *Prog. Oceanogr.* **40,** 337–369 (1998).
29. Ray, R. D., Eanes, R. J. & Chao, B. F. Detection of tidal dissipation in the solid Earth by satellite tracking and altimetry. *Nature* **381,** 595–597 (1996).
30. Ray, R. D. & Mitchum, G. T. Surface manifestation of internal tides in the deep ocean: observations from altimetry and island gauges. *Prog. Oceanogr.* **40,** 135–162 (1997).

Acknowledgements

We thank W. Munk for discussions. This work was supported by the US National Science Foundation (G.D.E.) and the US National Aeronautics and Space Administration (R.D.R.).

Correspondence and requests for materials should be addressed to G.D.E. (e-mail: egbert@oce.orst.edu).

A larger pool of ozone-forming carbon compounds in urban atmospheres

Alastair C. Lewis*†, Nicola Carslaw*, Philip J. Marriott‡, Russel M. Kinghorn‡, Paul Morrison‡, Andrew L. Lee*, Keith D. Bartle* & Michael J. Pilling*

** School of Chemistry, † School of the Environment, University of Leeds, Woodhouse Lane, Leeds LS2 9JT, UK*
‡ Royal Melbourne Institute of Technology, Department of Applied Chemistry, Melbourne 3001, Victoria, Australia

Volatile organic compounds play a central role in the processes that generate both urban photochemical smog and tropospheric ozone[1,2]. For successful and accurate prediction of these pollution episodes, identification of the dominant reactive species within the volatile organic carbon pool is needed[3]. At present, lack of resolution inherent in single-column chromatographic analysis[4] limits such a detailed chemical characterization of the complex urban atmosphere. Here we present an improved method of peak deconvolution from double-column (orthogonal) gas chromatography[5,6]. This has enabled us to isolate and classify more than 500 chemical species of volatile organic compounds in urban air, including over 100 multi-substituted monoaromatic and volatile oxygenated hydrocarbons. We suggest that previous assessments of reactive carbon species may therefore have underestimated the contribution made by volatile organic compounds to urban pollution, particularly for compounds with more than six carbon atoms. Incorporating these species in predictive models should greatly improve our understanding of photochemical ozone yields and the formation of harmful secondary organic aerosols[7,8].

Previous studies have shown that ozone production in urban areas of Europe is limited by the availability of volatile organic compounds (VOCs)[1]. Under these conditions, the concentration of ozone increases with that of VOCs, as demonstrated by standard ozone isopleth diagrams. Methods have been developed to rank the ability of individual VOCs to produce ozone, resulting in the US MIR scale[9] and the UK POCP scale[7]. Despite differences in definition, mode of calculation and emissions inventories, there is a broad general agreement on the relative ordering of different VOCs[7]. Generally, volatile aromatics have high reactivity (and hence POCP values), which increases with the degree of alkyl substitution. In addition to high photochemical reactivity, there is now strong evidence that the photochemistry of aromatic species can lead to the formation of secondary organic aerosols (SOA), which are known to